Quantitative ^{14}N NMR with Monte Carlo Uncertainty Analysis of Nitrate/Nitrite in Alkaline Nuclear Waste

Trent R. Graham,[A,*] Jacob Morton,[A] Ashley R. Kennedy,[A,B] Jacob G. Reynolds,[C] and Carolyn I. Pearce[A,D]

[A] Pacific Northwest National Laboratory, Richland, Washington 99354, USA

[B] Savannah River National Laboratory, Aiken, South Carolina 29808, USA

[C] Central Plateau Cleanup Company, LLC, Richland, Washington 99354, USA

[D] Crop and Soil Sciences Department, Washington State University, Pullman, Washington 99164, USA

* Corresponding author: trent.graham@pnnl.gov

ABSTRACT: Quantification of nitrate and nitrite concentrations is important for the management of radioactive tank waste chemistry, as these species influence solubility and corrosion. However, existing analytical methods are potentially hindered by turbidity, spectral interference, and delays from sample handling. We demonstrate quantitative ^{14}N nuclear magnetic resonance (qNMR) spectroscopy as a direct, matrix-tolerant approach for nitrate and nitrite detection at natural abundance. Monte Carlo resampling was integrated into the workflow to quantify marginal uncertainty, establish precision–time tradeoffs, and separate noise-limited uncertainty from systematic bias arising from shimming, transmitter offset, or excitation pulse conditions. Quantification of nitrate and nitrite was validated in controlled alkaline matrix challenges and in five multicomponent simulants of Hanford Waste. These results establish ^{14}N qNMR as a practical, uncertainty-bounded tool for quantifying redox-active nitrogen species in chemically complex environments and provide an approach for quantitative analysis of solution-state quadrupolar nuclei.

Introduction

Nitrate (NO_3^-) and nitrite (NO_2^-) are among the most abundant anions in alkaline radioactive waste, where they govern solubility equilibria, mass and charge balance, and bulk properties such as viscosity and density. [1-3] Both anions exert control on phase behavior, with nitrate in particular acting as a major component of both liquid and solid phases. [4] The presence of NO_3^- and NO_2^- can alter the solubility of mineral phases with no common ions, such as aluminum hydroxide ($Al(OH)_3$). [5-7] Radiolysis further converts NO_3^- to NO_2^-, ammonia, and nitrous oxide, altering solution chemistry in ways that link solubility and redox behavior across waste environments. [8,9] NO_3^- and NO_2^- are key species in the chemistry program to control corrosion of radioactive waste tanks at the Department of Energy's legacy nuclear site, Hanford. [10] NO_3^- and NO_2^- are present in high concentrations with the former acting as an aggressive species, and the latter acting as an inhibitor. Carbon steel corrosion due to NO_3^- is mitigated by addition of sodium hydroxide (NaOH), and chemistry control relies upon radiolysis to deplete NO_3^- to NO_2^-, which inhibits corrosion. In radioactive environments such as Hanford, the widespread occurrence and reactivity of NO_3^- and NO_2^- present both scientific challenges and operational risks. [11]

Applied analytical approaches are categorized as offline methods, which include separation-based techniques that typically require matrix manipulation, or online optical methods that are faster but susceptible to interference, such as turbidity. [12] Ion chromatography (IC) requires extensive sample handling. [13] Reverse-polarity capillary zone electrophoresis has also been applied to Hanford wastes reducing pre-analysis handling and secondary waste relative to IC, but still requiring dilution and offline operation. [14] Despite such improvements, offline approaches in radioactive environments still involve drawbacks including personnel exposure, personnel-intensive radiologically controlled sampling, and delays associated with safety protocols. [11] Online optical methods such as Raman, UV–Vis, and FTIR spectroscopy with chemometric analysis enable real-time monitoring. Raman spectroscopy, often supported by multivariate curve resolution, is notable for nitrate/nitrite detection, yet its performance can be constrained by turbidity, spectral overlap, and fluorescence. [12,15,16] Such limitations underscore the need for orthogonal techniques, and nuclear magnetic resonance (NMR) spectroscopy offers a promising alternative.

NMR spectroscopy provides isotope- and chemical-specific selectivity. [17] NMR spectroscopy is well established in process analytical technology for spin ½ nuclei such as ^{1}H, ^{13}C, ^{19}F and ^{31}P. [18] Applications to quadrupolar nuclei, such as ^{14}N, are less common, but there has been momentum in various applications (^{14}N, ^{27}Al, ^{33}S, ^{35}Cl, and ^{53}Cr). [19-29] While the ^{15}N nucleus (I = ½) yields sharp, quadrupole-free signals and is widely used for structural characterization, its low natural abundance (0.37%) and modest gyromagnetic ratio require isotopic enrichment or prohibitively long acquisition times. [30] In contrast, the quadrupolar ^{14}N (I = 1) nucleus is predominant at natural abundance (99.63%), but its rapid quadrupolar relaxation produces broad signals. [30] Early studies of ^{14}N NMR date back to the 1960s, and ^{14}N NMR Hanford-related work was detailed in the 1990s, with more recent ^{15}N NMR studies in simulants. [31-36] Despite these efforts, systematic application of quantitative ^{14}N NMR, particularly in multicomponent mixtures at high alkalinity representative of nuclear waste, remains limited.

Here we demonstrate that quantitative ^{14}N NMR, combined with Monte Carlo uncertainty analysis, enables direct, matrix-independent quantification of nitrate and nitrite at natural abundance. Monte Carlo resampling yielded parameter-specific confidence intervals, defined precision–time tradeoffs, while systematic bias arises from shimming, transmitter offset, and excitation conditions. Optimized protocols, including π/4 excitation, minimized these biases. The approach was validated in binary nitrite solutions, a ternary NaOH challenge designed to stress sensitivity under increasing alkalinity, and multicomponent Hanford-type simulants containing more than ten ionic species. Scaled signal to noise estimates were

propagated through Monte Carlo resampling to quantify calibration slope uncertainties. Together, these advances establish ^{14}N qNMR as an uncertainty-bounded, validated quantification approach for quadrupolar nuclei in complex environments.

Methods

Solution preparation

Multicomponent Hanford simulants were prepared as described in Schonewell et al. (2024).[37] These simulants consisted of a range of chemical components, including chromate [CrO_4^{2-}], aluminate [$Al(OH)_4^-$], oxalate [$C_2O_4^{2-}$], carbonate [CO_3^{2-}], sulfate [SO_4^{2-}], phosphate [PO_4^{3-}], nitrite [NO_2^-], nitrate [NO_3^-], chloride [Cl^-], fluoride [F^-], hydroxide [OH^-], calcium [Ca^{2+}], cesium [Cs^+], potassium [K^+], sodium [Na^+], strontium [Sr^{2+}], acetate [$CH_3CO_2^-$], and formate [CHO_2^-]. As detailed in the reference,[37] analyte concentrations within the simulants were quantified using Inductively Coupled Plasma-Optical Emission Spectrometry (ICP-OES) to determine the concentrations of Al, Ca, Cr, Na, and K. Following this, Inductively Coupled Plasma Mass Spectrometry (ICP-MS) was employed to measure the Cs and Sr content. Simulant anion loadings, including Cl^-, F^-, NO_3^-, NO_2^-, PO_4^{3-}, and SO_4^{2-}, were quantified using Ion Chromatography. The reagents used to make these simulants were of ACS Reagent Grade and a detailed table of these concentrations is provided in Table S1 of the *Supporting Information*. Additional samples comprising single-component $NaNO_3$ solutions were prepared by dissolving $NaNO_3$ (Sigma Aldrich, ACS Reagent Grade, ≥99%) in deionized water (18 MΩ·cm). Multicomponent $NaNO_2$ solutions in NaOH were prepared by first mixing $NaNO_2$ (Sigma Aldrich, ACS Reagent Grade, ≥96%) with NaOH (Sigma Aldrich, ACS Reagent Grade, ≥98%) in deionized water at the desired concentrations.

NMR spectroscopy

Nitrogen-14 NMR spectroscopy was performed on an 11.7534 T Avance III spectrometer (Bruker) equipped with a 5 mm BBO SmartProbe. The Larmor frequency of ^{14}N at 11.7534 T is 36.14 MHz. Spectra were acquired at 25 °C, unless otherwise stated. Typically, single-pulse, direct-excitation ^{14}N NMR spectra were acquired for calibration experiments using a $\pi/4$ pulse of ~ 22 µs. The transmitter offset was set at the midpoint between nitrate and nitrite resonances unless otherwise specified for offset sweeps. For the spectra underlying Monte Carlo analyses, the time domain size was 12048 points, with a sweep width of 30120.5 Hz, an acquisition time of 0.4 s, a recycle delay of 0.1 s, and up to 32768 transients. The effective recycle time per transient was defined as the sum of the acquisition time and the nominal recycle delay (aq + d1), which exceeded $5\times T_1$ for all ^{14}N measurements. Comparable acquisition settings were used for transmitter offset experiments, with systematic shifts of ~29 ppm. Likewise, for shim perturbation experiments a shift of z2 = ± 200 units was applied. For the spectra underlying quantitative ^{14}N NMR measurements of multicomponent, matrix-variable samples, conservative acquisition and recycle times were used (aq ≈ 4 s, d1 = 1 s), 32 transients, and a $\pi/4$ pulse. Frequency-domain processing included 20 Hz of exponential apodization (note intrinsic T_2 of NO_2^- is ~0.6 ms), zero-filling to 32768 points, and uniform baseline and integration windows. Experimental parameters for additional ^{1}H and ^{14}N experiments are provided in the captions of Figures S1, S2, S4, S5, and S8 in the *Supporting Information*.

For illustrative comparison of relative sensitivity, ^{15}N NMR spectroscopy was performed on an 11.7434 T NMR spectrometer (Agilent/Varian) equipped with a broadband probe. Spectra were acquired at 25 °C using single-pulse, direct-excitation experiments with a calibrated 45° pulse of 10.62 µs. The transmitter offset was set at the midpoint between nitrate and nitrite resonances. Each spectrum was collected with a

sweep width of 37 878.8 Hz, an acquisition time of 6.92 s, a recycle delay of 40 s, and 256 transients. To accommodate slow instrumental frequency drift over long acquisition times, experiments were implemented as pseudo-two-dimensional acquisitions and realigned prior to processing, with eight spectra of 256 transients co-added after alignment. Frequency-domain processing after addition included exponential line broadening of 2 Hz and baseline correction. The total experiment time was 26 h and 41 min.

Monte Carlo Assessment of Uncertainty

Monte Carlo resampling was used to quantify parameter-specific, marginal uncertainty.[38-40] Residuals from frequency-domain spectral fits were used to propagate uncertainty conditional on the processed spectrum and the observed noise scale. Residuals were computed as the difference between the fitted model and the processed spectrum, and their standard deviation was used as a single noise scale to generate Gaussian noise added in the frequency domain for Monte Carlo uncertainty propagation. Each synthetic spectrum was fitted with a pseudo-Voigt lineshape.[41] Pseudo-Voigt functions were used as flexible numerical models of the processed frequency-domain spectra rather than attempts to recover the underlying physical lineshape. Distributions of fitted values were compiled for peak position, linewidth, integral, and Gaussian factor. Properties of the resampled distributions of fitted values (mean and standard deviation) were extracted using Gaussian fits as an approximation. To extend results across different concentrations, uncertainties were scaled by integral-based signal to noise ratio (defined below). These scaled uncertainties were propagated into calibration slopes, producing distributions from which confidence intervals were derived. This Monte Carlo approach quantifies uncertainty conditional on the processed spectrum and does not explicitly model time-domain noise propagation or acquisition-level noise correlations, which are discussed in greater detail outside the scope of this work.[42] Estimates of precision were evaluated separately from bias effects introduced by controlled changes of shimming and transmitter frequency.

Here we extended the height-based signal to noise ratio,[43] to an integral-based signal to noise ratio (ISNR). ISNR was introduced here as an empirical normalization to compare uncertainty across resonances with substantially different linewidths, and was not intended as a formal estimator of analytical variance or independent noise samples. ISNR was defined as

$$\mathrm{ISNR} = \frac{I}{\sigma_R \sqrt{N_{\mathrm{eff}}}} \qquad \textbf{Eq. 1}$$

where I is the fitted signal integral, σ_R = standard deviation of residual, and N_{eff} = effective number of correlated points under the integration window, defined as the number of frequency-domain points within a total window of 5·FWHM (±2.5·FWHM around the peak center). N_{eff} is not interpreted as the number of statistically independent samples under apodization or other processing conditions that introduce correlated residuals. Throughout this work, signal quantitation is based on the analytic integral of the fitted pseudo-Voigt lineshape rather than numerical integration of discrete spectral points.

Distributions of pseudo-Voigt lineshape values were compiled for peak position, FWHM, I, and Gaussian factor. The relative standard deviation (RSD) of parameter i was defined as

$$\mathrm{RSD}_i(\%) = 100 \cdot \frac{\sigma_i}{\mu_i} \qquad \textbf{Eq. 2}$$

where σ_i and μ_i are the standard deviation and mean of integral, linewidth (FWHM), or Gaussian factor (G) obtained from the Monte Carlo resampling.

For peak position, given that the FWHM of nitrate and nitrite are significantly different, the FWHM-normalized standard deviation of peak position (NSD_p) was defined as

$$\mathrm{NSD}_p(\%) = 100 \cdot \frac{\sigma_\mathrm{p}}{\mu_\mathrm{FWHM}} \quad \textbf{Eq. 3}$$

Parameter-specific, noise sensitivity constants a_i were obtained by regressing RSD against ISNR with

$$\mathrm{RSD}_i = \frac{a_i}{\mathrm{ISNR}} \quad \textbf{Eq. 4}$$

In the noise-limited regime,[44] uncertainty decreases with the square root of the number of transients (nt) as

$$\mathrm{RSD}_i \propto \frac{1}{\sqrt{nt}} \quad \textbf{Eq. 5}$$

Finally, the number of transients and corresponding total acquisition time required at concentration (C) to achieve target precision of parameter i (TRSD_i) was calculated by ratioing a baseline dataset

$$t_{total} = t_0 \left(\frac{\mathrm{RSD}_{i,0}}{\mathrm{TRSD}_i}\right)^2 \left(\frac{C_0}{C}\right)^2 \quad \textbf{Eq. 6}$$

where t_0, C_0, $\mathrm{RSD}_{i,0}$ are the baseline measurement time, concentrations, and relative standard deviation, respectively. The reference dataset is that of nitrate for the nt=8192 acquisition (Table S6, *Supporting Information*). The measurement time is related to the recycle delay by the number of transients collected.

Results and Discussion

We benchmarked the relative sensitivity of ^{14}N and ^{15}N nuclei under process-relevant conditions to evaluate feasibility for direct nitrate/nitrite quantification. A prototypical 18-component matrix (S2; Na^+, K^+, Cs^+, $Al(OH)_4^-$, NO_3^-, NO_2^-, CrO_4^{2-}, F^-, PO_4^{3-}) was analyzed by single-pulse direct excitation for both nuclei. As shown in **Figure 1**, natural abundance ^{14}N produced NMR spectra with resolved NO_3^- and NO_2^- within seconds, whereas ^{15}N required acquisition times on the order of several days. The resonances of NO_3^- and NO_2^- were separated by ~233 ppm, nearly 20-fold larger than their FWHM (~1 ppm for nitrate and ~10 ppm for nitrite), providing baseline separation.

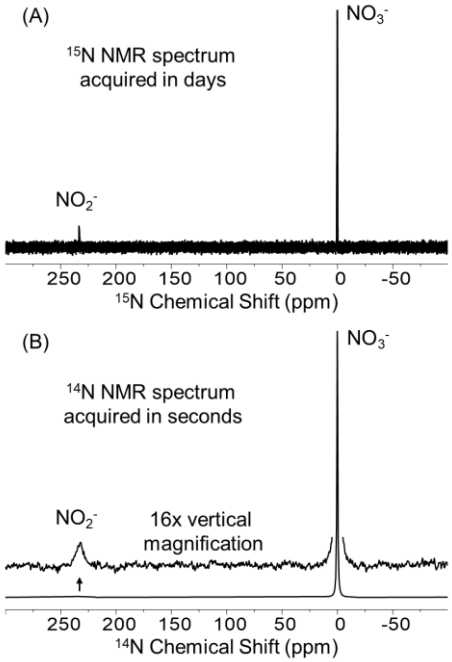

Figure 1. Nuclei-dependent signal acquisition rate. A comparison of natural abundance (A) ^{15}N and (B) ^{14}N NMR spectroscopy in the 18-component matrix, S2. The concentration of NO_3^- and NO_2^- are 3.64 M and 0.25 M (Table S1 in the *Supporting information*).

The large difference in signal acquisition rate arises from two factors. First, the high natural abundance of ^{14}N is 99.63% abundant whereas ^{15}N is 0.37%. Second, as detailed in Figures S1-S3 in the *Supporting Information*, the spin–lattice relaxation times (T_1) of NO_3^- and NO_2^- further enhance acquisition efficiency for ^{14}N relative to ^{15}N. In the prototypical 18-component S2 matrix, analysis of inversion recovery experiments[45] indicated that ^{14}N T_1 values were ~30 ms for NO_3^- and ~1 ms for NO_2^-. These T_1 values then facilitate selection of recycle delays of ~0.15 s, with the per-scan recycle time approximated as $5 \cdot T_1$. By comparison, the ^{15}N T_1 of a 1 M $Na^{15}NO_2$ standard was ~13 s, approximately two orders of magnitude longer than the ^{14}N values. On this basis, ^{14}N acquires at ~6.7 scans$\cdot s^{-1}$ compared to ~0.015 scans$\cdot s^{-1}$ for ^{15}N, corresponding to a ~430-fold rate advantage, independent of the disparity in natural-abundance of ^{14}N and ^{15}N.

Also described in Figures S4 and S5 in the *Supporting Information*, ^{14}N Carr–Purcell–Meiboom–Gill (CPMG) experiments[46] showed that the broader NO_2^- resonance arises predominantly from quadrupolar relaxation. The markedly shorter T_2 of NO_2^- (~0.6 ms) compared to NO_3^- (~32 ms) reflects the greater electric field gradient asymmetry at the nitrogen nucleus in a bent coordination (C_{2v}) in NO_2^-, relative to the trigonal planar (D_{3h}) coordination of NO_3^-.[47] Given that nitrite exhibits a sub-millisecond T_2, its quantitative reliability could be questioned.[48] This concern is investigated through analyses of precision-time and systematic bias, and ultimately resolved by demonstrating linear concentration dependence.

Monte Carlo Uncertainty Analysis

In solution, rapid isotropic tumbling averages the first-order quadrupolar interaction, while second-order quadrupolar effects contribute to rapid transverse relaxation, which, alongside post-acquisition processing, can result in broad observed lineshapes that are not well described by a strict Lorentzian model.[49] Quantitative analysis of ^{14}N NMR uncertainty and precision–time tradeoffs is not adequately

captured by conventional linear least-squares, as parameters of pseudo-Voigt line shapes can be coupled, such as FWHM and G. Likewise, since the Gaussian factor is bounded between 0 and 1 and post-acquisition apodization introduces correlated residuals, standard deviations from least-squares fits underestimate uncertainty and fail to capture covariance. [44] Accordingly, the Gaussian factor is treated as a statistical nuisance parameter retained to absorb model flexibility and stabilize estimation of the integral, linewidth, and peak position, rather than as a physically interpretable quantity. As shown in **Figure 2**, this limitation is evident in Monte Carlo ensembles at low transient (nt) averaging, where stacked spectra display broad noise manifolds not accounted for by least-squares error propagation.

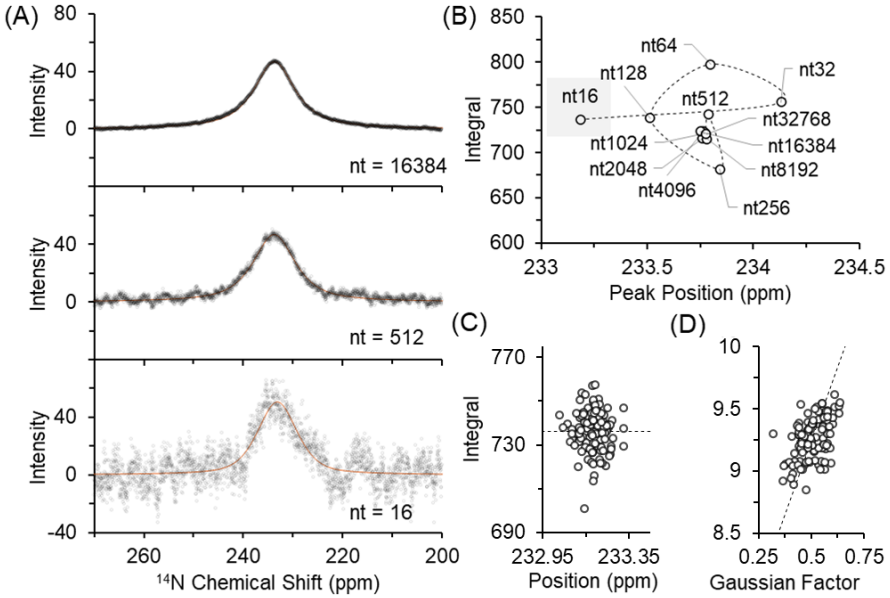

Figure 2. **Monte Carlo resampling of the fitted ^{14}N NMR spectra of the NO_2^- resonance in the S2 matrix. (**A) Stacked resampled spectra at low and high averaging illustrate noise behavior. (B) Mean integral and position values as a function of transients demonstrate convergence with averaging. (C) Parameter distributions of integral versus position at 16 transients demonstrate variance-limited scatter consistent with a two-dimensional Gaussian. (D) The relationship between FWHM and the Gaussian factor at 16 transients demonstrates parameter covariance. In panel B, the integral and peak position of the lowest-transient spectrum are highlighted in gray to guide the eye. In panels C and D, the line denotes the principal direction of variation of the Monte Carlo ensemble, constrained to pass through the ensemble mean. Comparable results for the NO_3^- resonance are provided in Figure S6 in the *Supporting Information*.

Residuals from fitted spectra were resampled using Gaussian perturbations scaled to the observed residual variance in the processed spectrum. Each synthetic spectrum was refit with the same pseudo-Voigt procedure. The resulting ensembles illustrate statistical behaviors. First, as shown in **Figure 2B**, the ensemble means of integral and peak position converge as the number of averaged transients increases. Second, with 16 transients, integral and peak position lead to an approximately Gaussian marginal uncertainty (**Figure 2C**) with the FWHM and the Gaussian factor having some degree of covariance, illustrating intrinsic coupling of those parameters in the pseudo-Voigt model. Unlike conventional nonlinear least-squares, Monte Carlo resampling propagates parameter covariance explicitly into marginal

uncertainty estimates,[40] for all parameters (see Tables S3-S7 in the *Supporting Information* for associated values).

When expressed as a function of the integral-based signal to noise ratio (ISNR; **Eq. 1**), marginal uncertainties for NO_3^- and NO_2^- collapsed onto common curves for normalized peak position (peak position/FWHM), along with the relative standard deviations of linewidth and integral (**Figures 3A–C**). On log-log axes, relative standard deviation values scaled linearly with ISNR (**Eq. 4**), with slopes of −1 within uncertainty, consistent with the expected noise-limited law, RSD ∝ 1/ISNR.[40] These relationships were evaluated by linear regression in log–log space after logarithmic transformation of both RSD and ISNR which yielded parameter-specific constants that quantify relative noise sensitivity (a_i, see Table S8 in the *Supporting Information*) with fitted intercepts corresponding to $\log(a_i)$. Among these, position exhibited the lowest constant, linewidth and integral were moderately more sensitive, and the Gaussian factor was far less stable. Unlike the other parameters, nitrate and nitrite did not collapse to a common curve for the Gaussian factor **(Figure 3D)**, reflecting its boundedness and covariance with linewidth. As a result, the Gaussian factor constants differed by orders of magnitude and exhibited wide confidence intervals, identifying the Gaussian factor as a statistical nuisance parameter, which stabilizes parameters of interest (integral, FWHM, and peak position).[41,50,51]

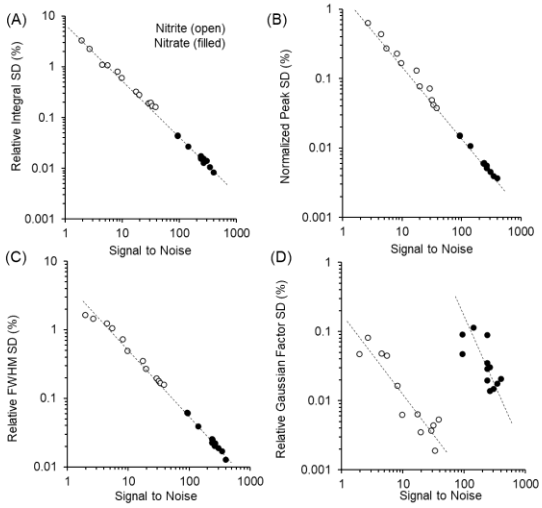

Figure 3. Scaling of marginal parameter uncertainty with the integral-based signal to noise ratio. The standard deviation of (A) integral, (B) position normalized by FWHM, (C) FWHM, and (D) Gaussian factor for NO_3^- and NO_2^-, fit separately due to boundedness and covariance with linewidth. Solid lines are log–log regressions of RSD or NSD according to **Eq. 3**, yielding slopes near −1 and intercepts corresponding to $\log(a_i)$ as shown in Table S8 in the *Supporting Information*.

Since the slopes in **Figure 3** are near −1, the data follow noise-limited scaling under the present acquisition and processing conditions for position, linewidth, and integral.[44] In contrast, deviations in Gaussian factor reflect large variability and instability, consistent with its identification as a statistical nuisance parameter.[41,50,51] Because the data fall in the noise-limited scaling regime, ISNR increases with the square root of the number of transients, and uncertainties follow the expected dependence within the noise-limited regime (**Eq. 5**).[44] This relationship underpins the acquisition planning chart (Figures S7, *Supporting Information*), which maps the concentration of NO_3^- or NO_2^- to the number of scans and total experiment time using **Eq. 6**, enabling scan/time predictions to be made from a single reference dataset.

For example, at 0.05 M concentration of either NO_3^- or NO_2^-, a ~0.1 h (6 minutes) and ~ 0.4 h (24 minutes) duration measurement achieves an integral with an RSD of 2% and 1%, respectively.

Bias analysis

Although random error decreases with averaging, systematic bias persists and must be evaluated separately. In these bias experiments, the objective was to assess systematic shifts in fitted parameter means rather than changes in measurement precision under degraded conditions. Shimming experiments quantified the influence of magnetic-field inhomogeneity on ^{14}N qNMR spectroscopy. For orientation, representative ^{1}H spectra illustrating severe shim distortions are provided in Figure S8 in the *Supporting Information.* For the corresponding ^{14}N spectra, distortion under the same shim conditions was significantly more modest and a pseudo-Voigt lineshape model was regressed. The ^{14}N peak position of nitrate (**Figure 4A**) shifted approximately linearly with z2, whereas linewidth broadened modestly and normalized integrals remained essentially constant within ±0.5% (**Figures 4B–C).** These results demonstrate that shim bias manifests primarily in line-shape parameters rather than in the integral. Operationally, this facilitates approximation of "acceptable" shims as those within ±500 z_2, under which the FWHM remains 31–34 Hz and normalized integrals vary by ≤0.5%. Notably, at these shim settings the corresponding ^{1}H spectra remain considerably distorted (Figures S8, *Supporting Information*), underscoring that the definition of "acceptable shims" is nucleus dependent.

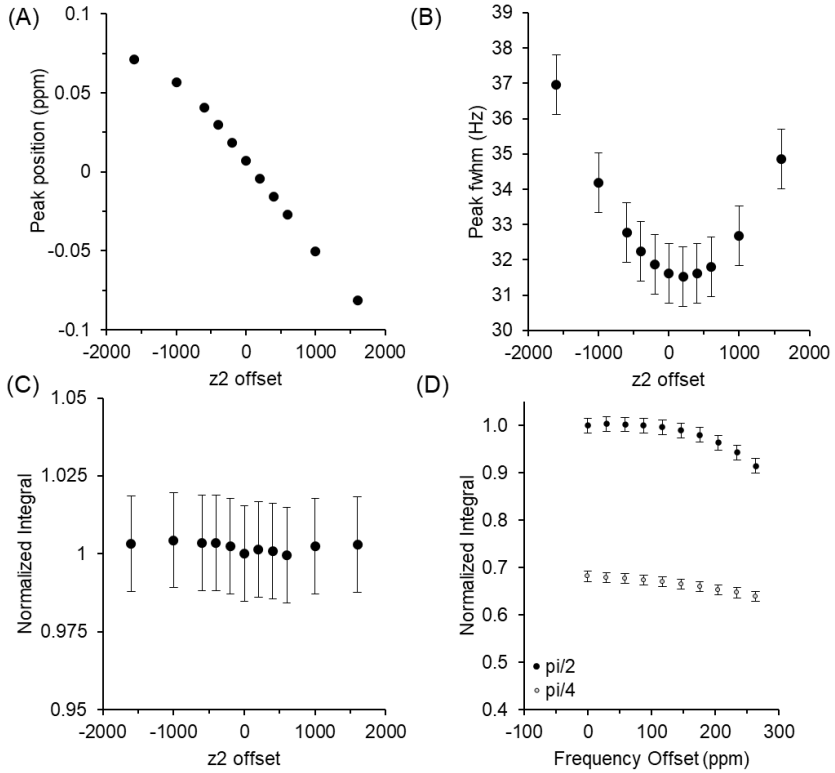

Figure 4. ^{14}N NMR spectroscopy of NO_3^- in the S2 matrix with bias introduced via shim malalignment and frequency offset. (A) Peak position as a function of shim offset (z2) showing an approximately linear trend. (B) FWHM as a function of z2 with near-parabolic dependence. (C) Normalized integral as a function of z2, invariant within ±0.5%. (D) Integral (normalized to z2 offset

of 0) as a function of transmitter offset for π/2 and π/4 excitation pulses. Error bars represent parameter uncertainty derived from Monte Carlo resampling of the unperturbed reference spectrum and are applied uniformly across all perturbed conditions to emphasize systematic bias effects.

Since NO_3^- and NO_2^- are separated by ~232 ppm at ~36 MHz, excitation bandwidth represents another source of systematic error.[25] Reduced RF power is required to suppress probe ringing over this dispersion, narrowing the excitation bandwidth and making apparent signal integrals dependent on excitation frequency.[52] To quantify this effect, integrals of the NO_3^- resonance in the S2 matrix were measured as a function of offset for π/2 and π/4 pulses (**Figure 4D**). At 300 ppm downfield from the NO_3^- resonance, π/2 excitation decreased the integrated resonance of NO_3^- by ~10%, whereas π/4 excitation decreased by ~6%. If the transmitter frequency is selected as the midpoint between the NO_3^- and NO_2^- resonances, each resonance lies within ±120 ppm from the center, and both excitations preserve quantitation within a few percent. Regardless, we selected π/4 excitation because it flattens the offset response, suppresses ringing, and yields more stable integrals. Although π/4 nominally reduces sensitivity by ~30% per scan, the short ^{14}N T_1 values (1–30 ms) ensure rapid recovery, so in practice the penalty is minimal for concentrations above the detection threshold. The same bandwidth and selectivity considerations extend broadly to multipulse experiments, which are generally susceptible to distortion when performed off-resonance.[49] Example multipulse experiments include inversion-recovery, saturation recovery, CPMG pulse sequences. To avoid such artifacts, measurements were performed with the transmitter frequency on-resonance for each analyte (Figure S1-S5, *Supporting Information*).

Quantitative Response Across Matrix Complexity

We further examined five multicomponent Hanford-type simulants (S1–S5, **Table S1**, *Supporting Information*) containing more than ten ionic species spanning millimolar to molar concentrations. Despite large differences in composition and ionic strength, integrated resonances of both NO_3^- and NO_2^- follow the same calibration line (**Figure 5**). For the five simulants at 25 °C, the calibrated ^{14}N π/2 pulse length varied by less than ~3% and the measured ^{14}N T_1 values for NO_3^- and NO_2^- were ≤ 80 ms (Figure S4 and S5, *Supporting Information*). This demonstrates that the method maintains quantitative performance across chemically diverse matrices and extends beyond controlled challenges to applied, multicomponent systems. Marginal uncertainty in these calibrations was quantified by Monte Carlo propagation of per-point measurement variances, derived from the linear fit using uncertainties established from the Monte Carlo analysis. The resulting slope was 3909 ± 20 counts·mM^{-1} (± 1σ).

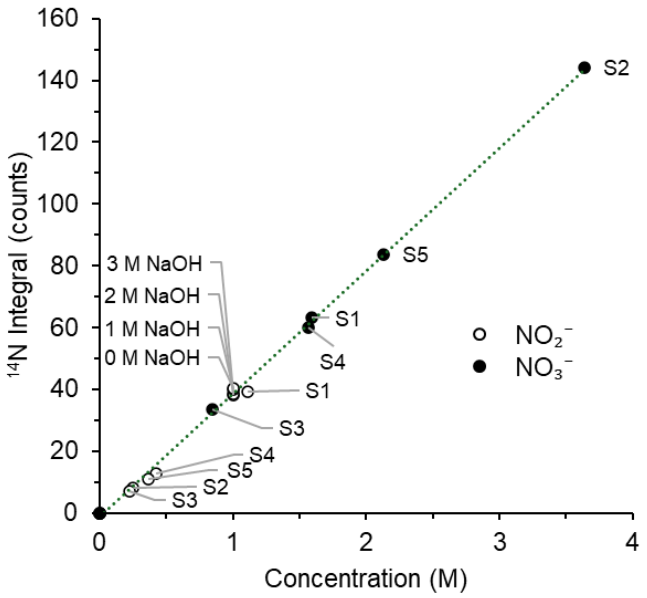

Figure 5. Quantitative response of ^{14}N qNMR across increasing matrix complexity and the matrix challenge of 0-3 M NaOH with 1 M $NaNO_2$.

We next assessed quantitative performance under controlled matrix perturbation by varying alkalinity in a ternary system ($NaNO_2$ + NaOH + H_2O). The NO_2^- ion was selected as the analyte because its shorter T_2 produces broader resonances and therefore provides a stringent test of quantitation. A $\pi/4$ excitation pulse was used to balance sensitivity with uniform excitation. Across the range of 0–3 M NaOH at fixed 1 M $NaNO_2$, all integrated intensities lie on a single calibration line within uncertainty (**Figure 5**). These results indicate that strong alkalinity does not degrade quantitative response. Within this bound, slopes were indistinguishable across the binary, ternary, and multicomponent cases, confirming that diverse matrix compositions did not affect the quantitative response of NO_3^- and NO_2^-.

Conclusions

This study establishes quantitative ^{14}N NMR as a practical approach for quantifying NO_3^- and NO_2^- concentrations in chemically complex environments. At natural abundance, ^{14}N provided rapid and quantifiable NO_3^- and NO_2^- signals, whereas ^{15}N required prohibitively long acquisition times. Monte Carlo analysis of marginal uncertainty was integrated to provide parameter-specific standard deviations for the integral, peak position, linewidth, and G, which facilitated ranking of their sensitivity to noise. The analysis clarified sources of systematic bias arising from shimming, transmitter offset, and excitation pulse bandwidth. Quantification of NO_3^- and NO_2^- was validated in binary, ternary, and multicomponent systems, including a controlled NaOH challenge and Hanford-type simulants with 18 ionic species. Despite deliberate perturbations and high ionic strength, NO_3^- and NO_2^- data converged to a single calibration. Marginal uncertainty estimates scaled for each matrix were propagated by Monte Carlo resampling of the calibration data points to yield statistically rigorous standard deviations for the calibration slope. Together, these results extend solution-state quadrupolar qNMR into chemically diverse environments and establish an uncertainty-bounded approach for advancing chemical quantification in complex environments.

Acknowledgements

This research was supported by IDREAM (Ion Dynamics in Radioactive Environments and Materials), an Energy Frontier Research Center funded by the U.S. Department of Energy (DOE), Office of Science, Basic Energy Science (BES) under FWP 68932. Graduate Fellows, A.K. and J.M., were supported by the Department of Energy Office of Environmental Management – Minority Serving Institutions Partnership Program (EM MSIPP). Carolyne Burns (PNNL) is thanked for providing the multicomponent Hanford Waste simulants. Peer reviewers are thanked for their constructive critique. A large language model assisted with language and editing. Pacific Northwest National Laboratory (PNNL) is a multiprogram national laboratory operated for DOE by Battelle Memorial Institute operating under Contract No. DE AC05-76RL0-1830.

Supporting Information Statement

Additional experimental details, NMR pulse sequence parameters, relaxation time measurements, Monte Carlo uncertainty analyses, multicomponent simulant compositions, and supporting NMR spectra.

References

1 Hill, R. C. P.; Reynolds, J. G.; Rutland, P. L. *A Comparison of Hanford and Savannah River Site High-Level Wastes*. In **Proceedings of the 13th International High-Level Waste Management Conference**; American Nuclear Society: La Grange Park, IL, 2011; pp 114–117.

2 Peterson, R. A.; Buck, E. C.; Chun, J.; Daniel, R. C.; Herting, D. L.; Ilton, E. S.; Lumetta, G. J.; Clark, S. B. Review of the Scientific Understanding of Radioactive Waste at the U.S. DOE Hanford Site. *Environ. Sci. Technol.* **2018**, *52*, 381–396. https://doi.org/10.1021/acs.est.7b04077

3 Reynolds, J. G.; Carter, R. Reconciliation of Solute Concentration Data with Water Contents and Densities of Multi-Component Electrolyte Solutions. *J. Solution Chem.* **2008**, *37*, 1113–1125. https://doi.org/10.1007/s10953-008-9296-9

4 Warrant, R. W.; Cooke, G. A. Characterization of the Solids Waste in the Hanford Waste Tanks Using a Combination of XRD, SEM, and PLM. *Adv. X-Ray Anal.* **2003**, *46*, 251.

5 Reynolds, J. G. Salt Solubilities in Aqueous Solutions of $NaNO_3$, $NaNO_2$, NaCl, and NaOH: A Hofmeister-like Series for Understanding Alkaline Nuclear Waste. *ACS Omega* **2018**, *3*, 15149–15157. https://doi.org/10.1021/acsomega.8b02052

6 Dembowski, M.; Snyder, M. M.; Delegard, C. H.; Reynolds, J. G.; Graham, T. R.; Wang, H.-W.; Leavy, I. I.; Baum, S. R.; Qafoku, O.; Fountain, M. S.; Rosso, K. M.; Clark, S. B.; Pearce, C. I. Ion–Ion Interactions Enhance Aluminum Solubility in Alkaline Suspensions of Nano-Gibbsite (α-$Al(OH)_3$) with Sodium Nitrite/Nitrate. *Phys. Chem. Chem. Phys.* **2020**, *22*, 24677–24685. https://doi.org/10.1039/C9CP05856G

7 Herting, D. L. *Effect of Phosphate, Fluoride, and Nitrate on Gibbsite Dissolution Rate and Solubility.* Technical Report LAB-RPT--13-00011-Rev.0; U.S. Department of Energy, Office of Environmental Management: Washington, DC, 2014. https://doi.org/10.2172/1119691

8 Horne, G. P.; Donoclift, T. A.; Sims, H. E.; Orr, R. M.; Pimblott, S. M. Multi-Scale Modeling of the Gamma Radiolysis of Nitrate Solutions. *J. Phys. Chem. B* **2016**, *120*, 11781–11789. https://doi.org/10.1021/acs.jpcb.6b06862

9 Murmu, M.; Saha, S. K.; Murmu, N. C.; Banerjee, P. Nitrate as corrosion inhibitor. In *Inorganic Anticorrosive Materials*; Verma, C.; Aslam, J.; Hussain, C. M., Eds.; Elsevier: Amsterdam, The Netherlands, 2022; pp 269–296.

10 Fuentes, R. E.; Wiersma, B. J.; Girardot, C. L.; Venetz, T. J.; Boomer, K. D. *Pitting Factor Criteria for Localized Corrosion Inhibition of Liquid Radioactive Waste Stored in Hanford Double Shell Tanks.* In **CORROSION 2019**; Association for Materials Protection and Performance: Houston, TX, 2019; Paper No. C2019-13430, pp 1–11. https://doi.org/10.5006/C2019-13430

11 Asmussen, R. M.; Bagwell, C. E.; Dixon, D. R.; Hare, L. R.; Johansen, S. K.; Johnson, C. D.; Meyer, P. D.; Pearce, C. I.; Plymale, A. E.; Saslow, S. A.; Szecsody, J. E.; Smith, G. L. *Nitrate and Nitrite at Hanford—From Tanks to Natural Attenuation*. Technical Report PNNL--35629; GLAW-RPT-003-Rev.0; Pacific Northwest National Laboratory: Richland, WA, 2024. https://doi.org/10.2172/2483349

12 Tse, P.; Bryan, S. A.; Bessen, N. P.; Lines, A. M.; Shafer, J. C. Review of On-Line and Near Real-Time Spectroscopic Monitoring of Processes Relevant to Nuclear Material Management. *Anal. Chim. Acta* **2020**, *1107*, 1–13. https://doi.org/10.1016/j.aca.2020.02.008

13 Connolly, D.; Paull, B. Rapid Determination of Nitrate and Nitrite in Drinking Water Samples Using Ion-Interaction Liquid Chromatography. *Anal. Chim. Acta* **2001**, *441*, 53–62. https://doi.org/10.1016/S0003-2670(01)01068-6

14 Okemgbo, A. A.; Hill, H. H.; Metcalf, S. G.; Bachelor, M. A. Determination of Nitrate and Nitrite in Hanford Defense Waste by Reverse-Polarity Capillary Zone Electrophoresis. *J. Chromatogr. A* **1999**, *844*, 387–394. https://doi.org/10.1016/S0021-9673(99)00291-5

15 Lines, A. M.; Bello, J. M.; Gasbarro, C.; Bryan, S. A. Combined Raman and Turbidity Probe for Real-Time Analysis of Variable Turbidity Streams. *Anal. Chem.* **2022**, *94*, 3652–3660. https://doi.org/10.1021/acs.analchem.1c05228

16 Foster, M.; Wharton, M.; Brooks, W.; Goundry, M.; Warren, C.; Storey, J. Remote Sensing of Chemical Agents within Nuclear Facilities Using Raman Spectroscopy. *J. Raman Spectrosc.* **2020**, *51*, 2543–2551. https://doi.org/10.1002/jrs.6016

17 Giraudeau, P. Challenges and Perspectives in Quantitative NMR. *Magn. Reson. Chem.* **2017**, *55*, 61–69. https://doi.org/10.1002/mrc.4475

18 Giraudeau, P. Quantitative NMR Spectroscopy of Complex Mixtures. *Chem. Commun.* **2023**, *59*, 6627–6642. https://doi.org/10.1039/D3CC01455J

19 Ruiz-Muelle, A. B.; Moreno, P. G.; Fernández, I. Quantitative Quadrupolar NMR (qQNMR) Using Nitrogen-14 for the Determination of Choline in Complex Matrixes. *Talanta* **2021**, *230*, 122344. https://doi.org/10.1016/j.talanta.2021.122344

20 Ruiz-Muelle, A. B.; Díaz Navarro, C.; Fernández, I. Quantitative Quadrupolar NMR (qQNMR) via Nitrogen-14 for the Accurate Control of L-Carnitine in Food Supplements. *J. Pharm. Biomed. Anal.* **2022**, *210*, 114548. https://doi.org/10.1016/j.jpba.2021.114548

21 Forte-Castro, A.; Ruiz-Muelle, A. B.; Fernández, I. Quantitative Quadrupolar NMR (qQNMR) Determination of Taurine in Undiluted Human Urine Samples Using 1D and 2D ^33S NMR. *Talanta* **2026**, *297*, 128556. https://doi.org/10.1016/j.talanta.2025.128556

22 Ruiz-Muelle, A. B.; Lestón-Cabeo, F.; Fernández, I. Accurate Detection of Perchlorate in Epoxy Resins via Chlorine-35 Quantitative Quadrupolar NMR (qQNMR). *Analyst* **2022**, *147*, 5075–5081. https://doi.org/10.1039/D2AN00759B

23 Graham, T. R.; Kennedy, A. R.; Morton, J.; Reynolds, J. G.; Pearce, C. I. Determining Hexavalent Chromium Transport Properties in Alkaline Nuclear Waste Using Nuclear Magnetic Resonance Spectroscopy. *Commun. Chem.* **2025**, *8*, 180. https://doi.org/10.1038/s42004-025-01546-7

24 Khatun, R.; Hunter, H. N.; Sheng, Y.; Carpick, B. W.; Kirkitadze, M. D. ^27Al and ^31P NMR Spectroscopy Method Development to Quantify Aluminum Phosphate in Adjuvanted Vaccine Formulations. *J. Pharm. Biomed. Anal.* **2018**, *159*, 166–172. https://doi.org/10.1016/j.jpba.2018.06.025

25 Wood, J. S.; Dal Poggetto, G.; Wang, X.; Reibarkh, M.; Williamson, R. T.; Cohen, R. D. Quantitative Nuclear Magnetic Resonance of Chloride by an Accurate Internal Standard Approach. *Magn. Reson. Chem.* **2023**, *61*, 22–31. https://doi.org/10.1002/mrc.5316

26 Deng, H.-L.; Luo, X.-S.; Lin, Z.; Niu, J.; Huang, M.-H. ^14N NMR as a General Tool to Characterize the Nitrogen-Containing Species and Monitor the Nitration Process. *J. Org. Chem.* **2021**, *86*, 16699–16706. https://doi.org/10.1021/acs.joc.1c01954

27 Sørensen, M. K.; Jensen, O.; Bakharev, O. N.; Nyord, T.; Nielsen, N. C. NPK NMR Sensor: Online Monitoring of Nitrogen, Phosphorus, and Potassium in Animal Slurry. *Anal. Chem.* **2015**, *87*, 6446–6450. https://doi.org/10.1021/acs.analchem.5b01924

28 Jensen, O. N.; Beyer, M.; Sørensen, M. K.; Kreimeyer, M.; Nielsen, N. C. Fast and Accurate Quantification of Nitrogen and Phosphorus Constituents in Animal Slurries Using NMR Sensor Technology. *ACS Omega* **2021**, *6*, 17335–17341. https://doi.org/10.1021/acsomega.1c01441

29 Feng, X.; Larson, R. A.; Digman, M. F. Evaluating the Feasibility of a Low-Field Nuclear Magnetic Resonance (NMR) Sensor for Manure Nutrient Prediction. *Sensors* **2022**, *22*, 2438. https://doi.org/10.3390/s22072438

30 Harris, R. K. *et al.* Further Conventions for NMR Shielding and Chemical Shifts (IUPAC Recommendations 2008). *Pure Appl. Chem.* **2008**, *80*, 59–84. https://doi.org/10.1351/pac200880010059

31 Witanowski, M.; Januszewski, H. ^14N Nuclear Magnetic Resonance: Amines and Ammonium Ions. *Can. J. Chem.* **1969**, *47*, 1321–1325. https://doi.org/10.1139/v69-217

32 Bobroff, S.; Phillips, R. J.; Shekarriz, A. *Nuclear Magnetic Resonance Measurement of Ammonia Diffusion in Dense Solid–Liquid Slurries*, Revision 1; Technical Report PNNL--11678-Rev.1; Pacific Northwest National Laboratory: Richland, WA, 1997. https://doi.org/10.2172/569011

33 Graham, T. R.; Wei, Y.; Walter, E. D.; Nienhuis, E. T.; Chun, J.; Schenter, G. K.; Rosso, K. M.; Pearce, C. I.; Clark, A. E. Tracking Nitrite's Deviation from Stokes–Einstein Predictions with Pulsed Field Gradient ^{15}N NMR Spectroscopy. *Chem. Commun.* **2023**, *59*, 14407–14410. https://doi.org/10.1039/d3cc04168a

34 Walter, E. D.; Schwarz, K. C.; Kumar, S. A.; Chen, Y.; Sassi, M.; Wang, Z.; Rosso, K. M. Evolution of Radicals from the Photolysis of High Ionic Strength Alkaline Nitrite Solutions. *J. Phys. Chem. A* **2020**, *124*, 3019–3025. https://doi.org/10.1021/acs.jpca.9b11438

35 Nienhuis, E. T.; Graham, T. R.; D'Annunzio, N. L.; Kowalska, M. I.; LaVerne, J. A.; Orlando, T. M.; Reynolds, J. G.; Camaioni, D. M.; Rosso, K. M.; Pearce, C. I.; Walter, E. D. Cations Impact Radical Reaction Dynamics in Concentrated Multicomponent Aqueous Solutions. *J. Chem. Phys.* **2023**, *158*, 224503. https://doi.org/10.1063/5.0153132

36 Salnikov, O. G.; Trofimov, I. A.; Bender, Z. T.; Trepakova, A. I.; Xu, J.; Wibbels, G. L.; Shchepin, R. V.; Koptyug, I. V.; Barskiy, D. A. Parahydrogen-Induced Polarization of ^{14}N Nuclei. *Angew. Chem. Int. Ed.* **2024**. https://doi.org/10.1002/ange.202402877

37 Schonewill, P.; El Khoury, L.; Burns, C.; Daniel, R. *Simulant Development of Potential 200 West Area Waste Feeds*. Technical Report PNNL-36628; Pacific Northwest National Laboratory: Richland, WA, 2024.
38 Guo, P.; Zhang, R.; Zhang, J.; Shi, J.; Li, B. A Monte Carlo Algorithm to Improve the Measurement Efficiency of Low-Field Nuclear Magnetic Resonance. *Sci. Rep.* **2023**, *13*, 10533. https://doi.org/10.1038/s41598-023-37731-8
39 Veen, A. M. H. van der; Cox, M. G. Getting Started with Uncertainty Evaluation Using the Monte Carlo Method in R. *Accred. Qual. Assur.* **2021**, *26*, 129–141. https://doi.org/10.1007/s00769-021-01469-5
40 Farrance, I.; Frenkel, R. Uncertainty in Measurement: A Review of Monte Carlo Simulation Using Microsoft Excel for the Calculation of Uncertainties through Functional Relationships, Including Uncertainties in Empirically Derived Constants. *Clin. Biochem. Rev.* **2014**, *35*, 37–61.
41 Ida, T.; Ando, M.; Toraya, H. Extended Pseudo-Voigt Function for Approximating the Voigt Profile. *J. Appl. Crystallogr.* **2000**, *33*, 1311–1316. https://doi.org/10.1107/S0021889800010219
42 Khirich, G. A. A Monte Carlo Method for Analyzing Systematic and Random Uncertainty in Quantitative Nuclear Magnetic Resonance Measurements. *Anal. Chem.* **2021**, *93*, 10039–10047. https://doi.org/10.1021/acs.analchem.1c00407
43 Hoult, D. I.; Richards, R. E. The Signal-to-Noise Ratio of the Nuclear Magnetic Resonance Experiment. *J. Magn. Reson.* **1976**, *24*, 71–85. https://doi.org/10.1016/0022-2364(76)90233-X
44 Bevington, P. R.; Robinson, D. K. *Data Reduction and Error Analysis for the Physical Sciences*; McGraw-Hill: New York, NY, 2003.
45 Torrey, H. C. Bloch Equations with Diffusion Terms. *Phys. Rev.* **1956**, *104*, 563–565. https://doi.org/10.1103/PhysRev.104.563
46 Meiboom, S.; Gill, D. Modified Spin-Echo Method for Measuring Nuclear Relaxation Times. *Rev. Sci. Instrum.* **1958**, *29*, 688–691. https://doi.org/10.1063/1.1716296
47 Schmidt, B. M.; Brown, L. C.; Williams, D. Chemical Shifts of ^{14}N in the NMR Spectra of Nitrates, Nitrites, and Nitro-Compounds. *J. Mol. Spectrosc.* **1958**, *2*, 551–557. https://doi.org/10.1016/0022-2852(58)90100-0
48 Chen, K. A Practical Review of NMR Lineshapes for Spin-1/2 and Quadrupolar Nuclei in Disordered Materials. *Int. J. Mol. Sci.* **2020**, *21*, 5666. https://doi.org/10.3390/ijms21165666
49 Levitt, M. H. *Spin Dynamics: Basics of Nuclear Magnetic Resonance*, 2nd ed.; John Wiley & Sons: Chichester, U.K., 2013.
50 Lee, S. M. S.; Young, G. A. Parametric Bootstrapping with Nuisance Parameters. *Stat. Probab. Lett.* **2005**, *71*, 143–153. https://doi.org/10.1016/j.spl.2004.10.026
51 Stancik, A. L.; Brauns, E. B. A Simple Asymmetric Lineshape for Fitting Infrared Absorption Spectra. *Vib. Spectrosc.* **2008**, *47*, 66–69. https://doi.org/10.1016/j.vibspec.2008.02.009
52 Jaeger, C.; Hemmann, F. EASY: A Simple Tool for Simultaneously Removing Background, Deadtime, and Acoustic Ringing in Quantitative NMR Spectroscopy—Part I: Basic Principle and Applications. *Solid State Nucl. Magn. Reson.* **2014**, *57–58*, 22–28. https://doi.org/10.1016/j.ssnmr.2013.11.002